https://doi.org/10.48048/tis.2022.6234

Passive Downward Heat Transfer in Reverse Thermosyphon Enabled Bubble Pump with Two Working Media for U-Tube Solar Thermal Collector

Arjun Kozhikkatil Sunil[1,*], Rakesh Kumar[2] and Tide Porathoor Sunny[3]

[1]National Engineering School of Gabes, University of Gabes, Omar Ibn Khattab 6029, Gabes, Tunisia
[2]Department of Mechanical Engineering, Indian Institute of Technology (ISM), Dhanbad 826004, India
[3]Division of Mechanical Engineering, School of Engineering, Cochin University of Science & Technology, Kalamassery 682022, India

([*]Corresponding author's e-mail: arjunks@cusat.ac.in)

Received: 28 July 2021, Revised: 21 September 2021, Accepted: 30 September 2021

Abstract

The study is aimed to evaluate the impact of multi-phase nanofluid flow to enhance heat transfer. The effect of liquid medium and pumping medium together with enabling a bubble pump to reverse thermosyphon arranged as an extension of the U-tube of solar thermal collector could affect a passive downward heat transfer numerically. The liquid and pumping medium selection were based on different nanofluid and phase change material accomplishment with respect to their optimal concentrations, optimal geometry of the reverse thermosyphon were compared. The occurrence of dry out limit and expansion boiling phenomena were identified by experimental work. The amount of optimal heat transfer in reverse thermosyphon was adjudged with respect to the thermal resistance, temperature between evaporator and condenser, fill ratio, tilt angle, heat transfer coefficient, thermal efficiency, etc. In this paper, the effects of major control parameters on thermal performance of passive heat transfer of solar energy are discussed.

Keywords: Thermal efficiency, CFD, Anti-gravity, PCM, Thermal storage, Nanofluid, Condensation, Evaporation

Nomenclature

A	Internal Cross Section Area	T_{ew}	Evaporator Wall Temperature
A_c	Surface Area Of The Solar Thermal Collector	T_s	Solar Thermal Collector Outlet Fluid Temperature
A_{mushy}	Mushy Zone Constant	U_L	Heat Transfer Coefficient Of Solar Thermal Collector
C_p	Heat Capacity	v	Velocity
d	Inner Diameter/Hydraulic Diameter	$\vec{v}$	Velocity Vector
f	Friction Factor	V_l	Volume Of The Liquid
g	Gravity Acceleration	Abbreviations	
F_R	Heat Removal Factor	CFD	Computational Fluid Dynamics
g	Gravity Acceleration	FR	Filling Ratio
G_T	Global Solar Radiation	HTC	Heat Transfer Coefficient
H	Internal Energy	HTF	Heat Transfer Fluid
h	Sensible Enthalpy	MWCNT	Multi Walled Carbon Nano-Tube
h	Heat Transfer Coefficient	NePCM	Nano Encapsulated Phase Change Material
h_e	Heat Transfer Coefficient At The Evaporator Section	PCM	Phase Change Material
h_{fg}	Latent Heat Of Vaporisation	PPM	Passive Pumping Module
h_l	Latent Heat of fusion	SIMPLE	Semi-Implicit Method For Pressure Linked Equations
I	Unit Tensor	SWH	Solar Water Heating
k	Thermal Conductivity	THP	Thermosyphon Heat Pipe

l_e	Length Of The Evaporator Zone
Nu	Nusselt Number
p	Pressure
Q	Overall Rate Of Heat Transfer / Power Throughput
Q_e	Input Power
R	Thermal Resistance
R_c	Condenser Thermal Resistance
R_e	Evaporator Thermal Resistance
Re	Reynolds Number
S_g	Source Term
t	Time
T_b	Arithmetic Average Of Outlet And Inlet Temperatures
T_c	Condenser Average Wall Temperature
T_{cv}	Vapour Temperature At The Condenser
T_{cw}	Condenser Wall Temperature
T_e	Evaporator Average Wall Temperature
T_{ev}	Vapour Temperature At Evaporator Section
TPCT	Two Phase Closed Thermosyphon
TS	Temperature Sink
UDF	User Defined Function

Greek Symbols

ΔH	Latent Heat
ΔP	Pressure Drop
$\dot{m}$	Fluid Flow Rate
α	Absorptance Of The Absorber Plate
β	Liquid Fraction
η_{th}	Thermal Efficiency
μ	Dynamic Viscosity
ρ	Density
$\vec{\tau}$	Stress Tensor
τ_a	Ambient Temperature
τ_i	Inlet Fluid Temperature
τ_o	Outlet Fluid Temperature
τ_{ap}	Transmittance-Absorptance Product

Introduction

In a solar thermal collector, the selective coating on the evacuated tube inner cover converts solar energy into heat energy and transfers the heat using an aluminium fin to the copper U-tube [1-8]. Although fins increased heat transfer through natural convection [9], they confined the vortex domain of natural convection. The liquid (a mixture of water and phase change material) in the U-tube is heated and conducts the heat energy to the water through a bubble pump enabled reverse thermosyphon. Traditional working media (HTFs) such as ethylene-glycol have a high boiling point of 197 °C, high thermal conductivity, and high specific heat capacity [10,11]. However, for a medium-high operating temperature U-tube evacuated solar thermal collector system, ethylene glycol/pure water working media are not desirable as they have a lower boiling point of approximately 107 °C [10]. Using water as the working media in a U-tube evacuated solar thermal collector with medium-high operating conditions could pose problems such as the evaporation of water at approximately 100 °C, which causes the working media to lose energy. Additionally, it could also cause an increase in pressure of the tubes, which could potentially lead to issues relating to the pumping effect of water working media throughout the system.

Modern solar water heating technology has the storage unit which is PCM-based designed as a separate medium away from the solar thermal collectors. The energy storage materials widely studied are triacontane paraffin ($C_{33}H_{68}$). Studies using erythritol ($C_4H_{10}O_4$) as working media [12-16] are also reported. Erythritol has high latent heat properties, exceptional specific heat capacity than paraffin wax, non-toxic, and has good thermal conductivity properties, inexpensive and easily available.

As erythritol crystallizes from liquid to solid form, the material goes through a significant volumetric expansion of approximately 14 % and this sub-cooling effect (reduction in heat released back into the system) allows for erythritol to maintain in liquid form for more period of time before crystallizing [17,18]. Erythritol has a higher melting temperature compared to traditional working media such as water and glycol which is a desirable property as it will hold more heat, and hence can heat up to a higher temperature. The reliability of positive effects from the inclusion of nanoparticles depends on the stability of a homogenous mixture and the use of dispersants has been shown to improve the stability and homogeneity of nanoparticle-doped erythritol mixtures. Thermal expansion of erythritol during crystallization could lead to the breakage of copper tubes and hence should be avoided. The addition of MWCNT nanoparticles with a small amount of tri ethanol amine dispersant further increases the thermal conductivity and specific heat capacity of erythritol [19]. Besides, there is also a decrease in freezing onset temperature (sub-cooling) of approximately 5 °C leading to the prolonged time remaining in liquid form. The latent heat of fusion of erythritol is enhanced with the addition of MWCNT nanoparticles. During the day when the tube is exposed to sunlight, solar energy is absorbed by the solar selective coating, which effectively heats up the working

media ready for use in the U-tube [20,21]. Due to supercooling a PCM can exist in the liquid form without fully freezing below the phase change temperature or its freezing point [22-25].

The present study will evaluate the impact of using nanofluids and enhancing the heat transfer fluid temperature, and using PCM in improving the heat transfer by using a 2D model of a single U-tube integrated evacuated solar thermal collector through a bubble pump enabled reverse thermosyphon numerically considering multi-phase flow. Nanofluids were selected because they have better thermal properties and can increase the heat transport because of turbulence effect of brownian nanoparticle movement. Water with different concentrations of TiO_2, CuO, SiO_2, Al_2O_3, Ag, and MWCNT nanoparticles will be used as working media, using tri ethanol amine as the dispersant, and erythritol will be utilized as PCM. Studies will be conducted on a finned U-tube for the solar heat flux of 100 - 500 W at tilt angle 50 - 70 °C at Re 500 - 30,000. Nanofluids will be filled to a different volume of the evaporator section (i.e. FR = 0.5 - 1). The present study will use a combination of the storage and heat transfer both in a single unit, in which the U-tube effectively replaces the thermosyphon. Major problems such as the increase of energy consumption and temperature variations thus limit practical applications. The aluminum fin will be considered as part of a conduction layer defined in FLUENT with a thickness of 0.2 mm. The U-tube will be defined as copper tubing with a wall thickness of 0.1 mm. A simple condenser section will be created by extending one side of the U-tube geometry where the working media in the U-tube transfers heat to heat water as if in a simple heat exchanger configuration. The visualisation of multi-phase flow along with the behaviour of heat transfer analysis, pool boiling process, phenomena of film condensation, temperature distribution profiles, and thermal performance of CFD simulations of reverse thermosyphon filled with water and various nanofluids will be presented in this paper. Simple experimental work will also be conducted using a simple heat pipe of similar geometry as that of the bubble pump enabled reverse thermosyphon with similar boundary conditions to adjudge the phenomena in the vapour transport to condenser and its return after condensation in respect of the nanofluid in comparison to the operation with water.

Materials and methods

Theory

Governing equations of momentum, energy, and continuity equations were simultaneously solved and the continuity equations are defined in Fluent [26]. The continuity equation is defined as:

$$\frac{\partial \rho}{\partial t} + \nabla(\rho \vec{v}) = 0 \tag{1}$$

$\vec{v}$ and ρ denotes the velocity vector and density.

Meanwhile, the momentum equation is defined as:

$$\frac{\partial}{\partial t}(\rho \vec{v}) + \nabla(\rho \vec{v}\vec{v}) = -\nabla p + \nabla \vec{\tau} + \rho \vec{g} + S_g \tag{2}$$

τ is the stress tensor, p denotes the pressure and g is the acceleration due to gravity. Lastly, the energy equation for melting/solidification problems is written as below:

$$\frac{\partial}{\partial x}(\rho H) + \nabla\big(\vec{v}(\rho H + p)\big) = \nabla(k\nabla T + \vec{\tau}\vec{v})S_H \tag{3}$$

H is the internal energy, the sum of sensible enthalpy h and latent heat ΔH of the PCM, and k is the thermal conductivity.

$$\Delta H = \beta h_l \tag{4}$$

β is the liquid fraction of the PCM and h_l is the latent heat of fusion. In Fluent the liquid fraction β is defined as:

$$\beta = 0, if\ T < T_{solidus} \tag{5}$$
$$\beta = 1, if\ T < T_{liquidus} \tag{6}$$

$$\beta = \frac{T - T_{solidus}}{T_{liquidus} - T_{solidus}}, if\ T_{solidus} < T < T_{liquidus} \tag{7}$$

Furthermore, the stress tensor $\vec{\tau}$ the equation is as follows:

$$\vec{\tau} = \mu\left[(\nabla\vec{v} + \nabla\vec{v}^T) - \frac{2}{3}\nabla\cdot\vec{v}I\right] \tag{8}$$

In which I is the unit tensor and μ is molecular viscosity. Finally, for natural convection and mushy region, the source term S_g was considered as follows [27]:

$$S_g = \rho\vec{g}\beta(T - T_{ref}) - \frac{(1-\beta)^2}{\beta^3 + \epsilon}A_{mushy}\vec{v} \tag{9}$$

The second term in equation 9 relates to the porosity of the porous medium in each cell where the liquid fraction is considered [27]. The mushy zone constant A_{mushy} is set at 100000 (mushy zone is the mixed solid-liquid region). Meanwhile, to avoid a division by zero, ϵ was set as a very small number of 0.001 [26].

The heat removal factor (F_R) of solar thermal collector demarcate the fraction of actual to maximum heat transfer. Maximum value of heat transfer is obtained when the heat loss is minimum to the surrounding and as the solar thermal collector temperature approaches the inlet fluid temperature. The equations used for evaluation of the instantaneous thermal efficiency (η_{th}) of the solar thermal collector is that of Hottel-Whillier-Bliss [28-30], using the modified efficiency curve model. The radiation absorbed by the absorber can be assumed to be the transmittance-absorptance and incident radiation product $(\tau_{\alpha p})$.

F_R is the heat removal factor, the absorptance of the absorber (α) cover transmittance (τ), overall solar collector heat transfer coefficient (U_L, W/m^{2}K), inlet fluid temperature of the solar thermal collector (τ_i, K), ambient temperature (τ_a, K) and global solar radiation (G_T, W/m^2). The relationship of each parameter is given as follows [31,32]:

$$\eta_{th} = \frac{Q}{A_c G_T} = \frac{\dot{m}C_p(\tau_0 - \tau_i)}{G_T} \tag{10}$$

Q is the useful solar energy rate gained to the thermal collector (W), $\dot{m}$ is the fluid flow rate (l/hr), C_p is the heat capacity of the circulating fluid (J/kgK), τ_i and τ_0 are the temperature (K) of the inlet and outlet respectively, A_c is the collector surface area (m^2).

$$\eta_{th} = F_R\tau_a - F_R U_L\frac{(\tau_i - \tau_a)}{G_T} \tag{11}$$

The solar thermal collector with bubble pump enabled reverse thermosyphon is used such that the nanofluid closed circulation is maintained with a tilt angle of 65°. Fluid inlet, surface, ambient, and outlet temperatures, friction factor, wind velocity, and global solar radiation are found. The nanofluid flow rates are varied in the solar thermal collector for the study. The Reynolds number in the collector $(Re = 4\dot{m}/\pi d\mu)$ of nanofluids with a viscosity (μ) and is estimated with respect to the tube hydraulic diameter or tube inner diameter (d).

The escalated fluid resistance leads to pressure drop reduction across the tube, and the same is employed in friction factor estimation.

$$f = \frac{\Delta P}{\left(\frac{L}{d}\right)\left(\frac{\rho V^2}{2}\right)} \tag{12}$$

Where L is the tube length (mm), ΔP is the pressure drop, v is velocity and ρ is density.

The Nusselt number is analyzed as follows:

$$Nu = \frac{hd}{k} \tag{13}$$

Where the heat transfer coefficient (W/m^2K) $h = Q/A_c(T_s - T_b)$, T_s is solar thermal collector outlet fluid temperature after time t, T_b is arithmetic average of outlet and inlet temperatures, k is the thermal conductivity (W/mK). $A_c = \pi dL, T_s = T_1 + T_2 + T_3/3$ and $T_b = T_o + T_i/2$.

The transmittance for the visible wavelength range and the absorptance of the absorber plate are $\tau = 0.89$ and $\alpha = 0.89$, respectively.

The thermal resistance is an important parameter of the heat transfer performance of the tube pipe. Thermal resistance of the evaporator (°C/W) is defined as:

$$R_e = \frac{T_{ew} - T_{ev}}{Q_e} \tag{14}$$

T_{ew} is the wall temperature of the evaporator, T_{ev} is vapour temperature of the evaporator and Q_e is the power input.

Thermal resistance of the condenser is:

$$R_c = \frac{T_{cv} - T_{cw}}{Q_e} \tag{15}$$

T_{cw} is the wall temperature of the condenser, Q_e is the input power and T_{cv} is condenser vapour temperature.

Thermal resistance of tube pipe is [33]:

$$R = \frac{T_{ew} - T_{cw}}{Q_e} \tag{16}$$

Heat transfer coefficient of evaporator $(W/m^{2\circ}C)$ is:

$$h_e = \frac{Q}{A(T_{ew} - T_e)} \tag{17}$$

The performance of the CFD simulation of thermosyphon is illustrated by the thermal resistance on an overall basis. Heat transfer of the overall system is proportional to effective temperature difference of condenser and evaporator, but the relationship with the thermal resistance is established reciprocally.

Heat transfer rate on an overall basis is:

$$Q = \frac{T_e - T_c}{R_{eq}} \tag{18}$$

where T_e and T_c depicts evaporator as well as condenser mean temperatures at the wall, sequentially, R represents thermal resistance (K/W) and Q is power throughput.

The filling ratio can be calculated as:

$$FR = \frac{V_l}{Al_e} \times 100 \tag{19}$$

A is internal area of pipe, l_e is evaporator length, and V_l is liquid volume.

CFD Modelling

In the FLUENT solver, a pressure-based solver was utilized and the SIMPLE algorithm scheme with PRESTO! mode was used. The least square cell-based method was used to solve for the gradient with second-order upwind mode used to solve for momentum and energy. Meanwhile, convergence criteria of 10^{-6} was selected for continuity and momentum while the convergence criteria of 10^{-8} was selected for energy equations. For solution control methods, liquid fraction, momentum, and pressure were under-relaxed by factors of 0.9, 0.5, and 0.3, respectively in order to achieve stable convergence. The simulation ran for 3 h using a time step size between 0.1 and 1 s based on convergence. The evaporator section is indicated by the distance between 0 and 200 mm, the condenser section is indicated by the distance between 300 and 500 mm and the adiabatic section is indicated by the distance between 200 and 300 mm.

A user-defined function (UDF) was also created to record and store average temperature at the surface of the outlet of the U-tube. This UDF code records temperature at the surface of the outlet of the U-tube to be used as the inlet temperature of the U-tube for the following iteration, creating a closed-loop piping system. The operation of change in phases occurring in the course of evaporation as well as condensation was simulated in FLUENT due to the flexibility and accuracy of the finite volume method. Through user-defined functions, the change in phase simulation ability could be enhanced in FLUENT by the development of an in-house code during a reverse thermosyphon operation.

The simulation was conducted with constant heat flux. A solar thermal collector is practiced as the source of heat of reverse thermosyphon. Thermosyphon is placed above the solar thermal collector. Reverse thermosyphon having 2 working media (**Figure 1**) consist of a U-tube (U) with a fin (F) of the solar thermal collector providing heat flux, bubble pump (B), an evaporator (E), an adiabatic section (S), and a condenser (C); which are interconnected to become a closed system of liquid. **Figure 1** shows the schematic diagram of reverse thermosyphon with 2 different working media. The evaporator has liquid medium (LM), performing the transfer of heat and pumping medium (PM), filled partly. Thin film of the pumping medium of 9 - 10 mm on the bulk of the liquid medium is introduced as a layer. An inlet valve transfers the pumping medium upon vaporization and under optimum pressure to the bubble pump. As it passes to the adiabatic section (separator) from the evaporator, the liquid and pumping media are separated, and by gravity, the liquid medium enters back to the evaporator along with a portion of vaporized liquid medium cooled in the condenser also is redistributed to evaporator section. Vaporized PM with condenser entry status reaches evaporator by gravity. Heat is transferred to the collector from the evaporator by natural convection with the liquid and pumping media. Liquid medium shows maximum flow rate during slug flow [34] in a 2-phase study of a bubble pump.

For this study, CFD simulation of the system in stagnation (on-demand) operation was investigated. Stagnation operation can be defined such as there is no circulation of working media throughout the system as the evacuated solar thermal collector absorbs solar radiation during the day, allowing the evacuated solar thermal collectors to achieve maximum energy storage that can be used when circulation of working media is initiated in the system at a later time of the day [35]. Stagnation operation only has approximately 3 h worth of simulation data whereas the normal operation (where working media circulates the system all day) has 24 h worth of simulation data. As this is a completely new system that is being studied with no prior experimental work or data, preliminary analysis in stagnation operation effectively reduces overall computational time.

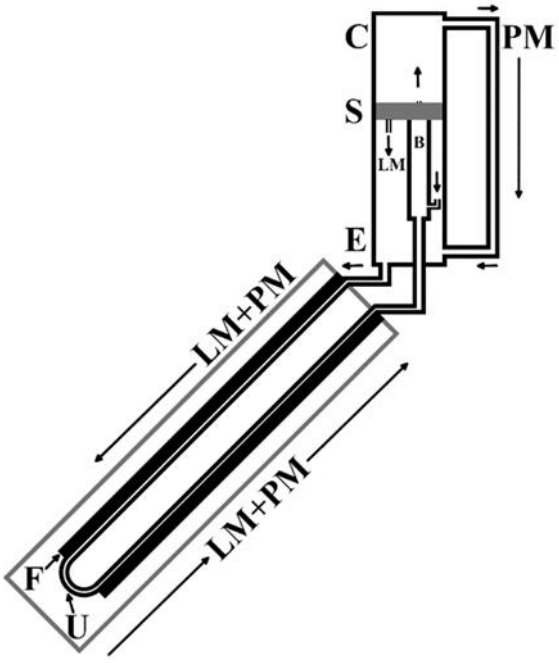

Figure 1 Circuit diagram of bubble pump enabled reverse thermosyphon with 2 working media.

Mesh geometry and independence

An air domain was defined inside the collector between the glass, reflector, and receiver for the calculation of the free convection, fluid flow, and radiation field. Some of the small parts of the collector were not considered to simplify the geometry. ANSYS meshing tool was used to generate the 2D mesh (**Figure 2**). The space around the reflector, the receiver, and the surrounding edges were meshed carefully due to the strong temperature and velocity gradients. The elements of quadrilateral shape were employed for meshing (**Figure 2**), so as to enable the time for simulation shorter for simple geometries. As the number of elements increase after 2 lakhs when we observe from 1.5 lakhs up to 2.5 lakhs, the heat flux is not seen modified. The accuracy with respect to convergence upon mesh independence is observed through an analysis of grid sensitivity, using a 2-dimensional model of rectangular structure made in ANSYS. The heat flux simulations are carried out at the wall for natural convection in a fluid consisting of Ag nanoparticles dispersed in water. A mesh density element of 2 lakh, hence would be ideal with respect to the numerations.

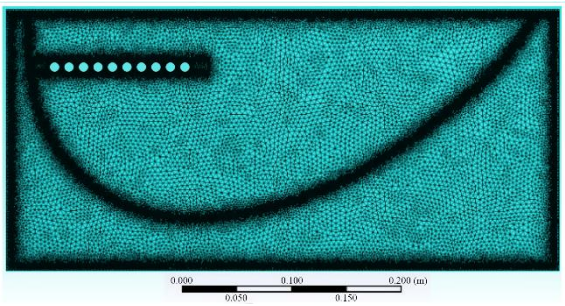

Figure 2 Mesh of solar thermal collector.

To achieve uniform mesh, the geometry is divided into 4 different parts and applying a combination of hexahedral and tetrahedral meshes. The U-tube geometry is further divided as an orthogonal-grid (O-grid) mesh using hexahedral meshes (**Figure 3**), which are often desirable when analyzing a flow with heat transfer problem in a cylindrical pipe as it allows for users to have better control over the mesh quality as well as yielding to the best distribution of mesh, as reported by Hernandez-Perez *et al*. [36]. Inflation layers around the walls of the U-tube were applied to ensure that the melting and solidification behaviour of material closer around the U-tube walls can be captured. For the PCM region, tetrahedral meshes were used by applying body sizing with element sizes of 0.002 m. A total of 416,398 nodes were generated for this model. To ensure sufficient quality of the mesh generated, mesh skewness and mesh orthogonal quality was monitored where the minimum orthogonal quality was kept to be >0.1 and the maximum skewness was maintained <0.9.

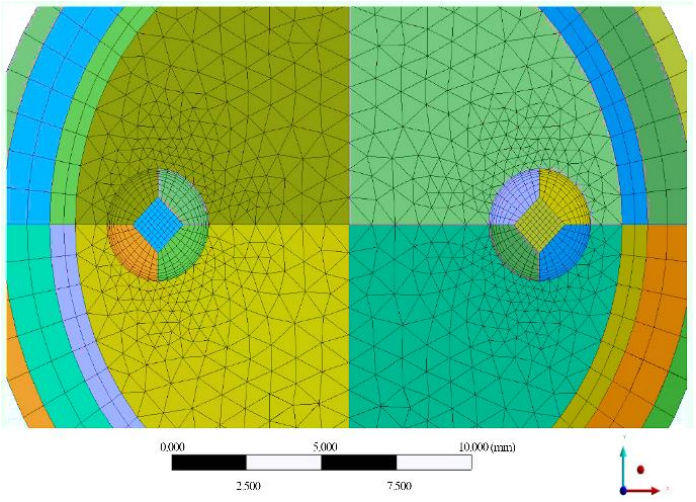

Figure 3 Mesh of U-tube.

GAMBIT software is used to generate the 2-dimensional geometry of reverse thermosyphon and subsequent meshing. The 1st grid size was 0.01 mm and the growth ratio was 1.2. A single layer of cells with 36 cells is considered for the walls at the bottom and upper positions with adiabatic nature. For grid independence studies, various sizes of mesh are utilized. The mean temperature values for all the 3 different sections, using water as the working media, such as evaporator, adiabatic, condenser sections are monitored. Fifteen cell layers are selected for analyzing the film of liquid getting developed near the left and right wall regions (**Figure 4**).

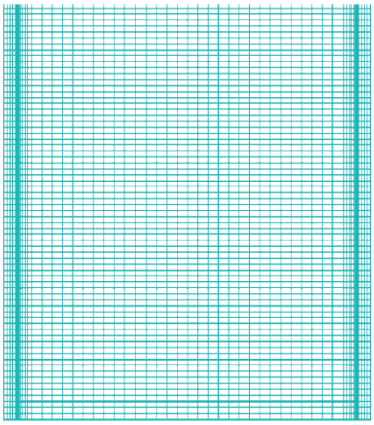

Figure 4 Mesh of reverse thermosyphon.

The results of grid-independence for the reverse thermosyphon containing water for heat input of 100 W for a mesh size of 19,500 (cells) shows that the 3 different sections of the reverse thermosyphon, namely the evaporator, adiabatic section, and condenser registered mean temperatures of 30.51, 26.03, and 21.48 °C, respectively and that for a mesh size of 69276 were 29.16, 25.86 and 22.45 °C, respectively and that for a mesh size of 129,944 were 29.32, 25.89 and 22.47, respectively. Thus, the mesh size selected for the numerical study is 69,276. The solid region contains 15092 cells and 54184 quad cells for the fluid region. As a result, 69,276 cells are generated. Fifteen cell layers are selected to analyze the film of liquid getting developed near the left and right wall regions. The mesh sizes of 69,276 and 129,944 revealed very similar values of mean temperature for evaporator, adiabatic, and condenser sections of the reverse thermosyphon.

Initial and boundary conditions

Boundary conditions of solar thermal collector

The details of the solar thermal collector with respect to its boundary conditions are listed in **Table 1**. The equations for the evaluation of the performance of the collector using nanofluids are given below.

Table 1 Boundary conditions of solar thermal collector.

Solar radiation	≥ 810 W/m^2
Wind speed	2.1- 4.3 m/s
Maximum variation in flow rate	0.001 %
Maximum variation in fluid inlet temperature	29.6 °C
Maximum variation in temperature at the inlet	1 °C
Inner tube diameter	8 mm

Boundary conditions of the U-tube

The solution of mass and momentum of flows with respect to conservation of equations was carried out using ANSYS Fluent. Energy conservation was also solved in this case as this is a heat transfer

simulation. Moreover, the melting/solidification model was used to portray the melting/solidification behaviour of the PCM. To simplify the model, several assumptions were made following the simulation:

- No heat loss or gain from the surrounding.
- Flow in the U-tube is laminar, steady and incompressible.
- Constant thermophysical properties of PCM.
- Boussinesq approximations are assumed to be valid for density variation of PCM to aid in faster convergence for natural convection flows.
- A user-defined function (UDF) was also created to record and store average temperature at the surface of the outlet of the U-tube. This UDF code records temperature at the surface of the outlet of the U-tube to be used as the inlet temperature of the U-tube for the following iteration, creating a closed-loop piping system.
- The vacuum region was defined as having properties of air but with very low thermal conductivity and very low specific heat capacity to prevent any heat transfer through conduction. The temperature of the vacuum is also set as a fixed value of 298 K throughout the simulation.

Boundary conditions of the reverse thermosyphon

- Constant heat flux at evaporator wall with non-slip at inner walls.
- Zero heat flux at upper and lower ends as well as at adiabatic section.
- Convection heat transfer with heat transfer coefficient values from the CFD simulation of the condenser at the walls of the condenser.
- Interfaces between fluid and solid regions of the heat pipe are assumed as a boundary condition of the coupled wall for allowing the heat transfer between the zones of fluid and solid.
- Due to time constraints, physical properties at 298.15 K are considered and assumed temperature independent except density and surface tension of liquid phase.

Validation

As shown in **Figure 5** as the heat flux increases from 100.41 to 376.14 W/m^2 the temperature between evaporator and condenser for computational results was compared with the results of experimental work [37] and observed that the temperature increases, whereas the thermal resistance decreases. The deviation percentage for temperature between evaporator and condenser for experimental and computational is 3.7 %. For temperature between evaporator and condenser, the highest deviation between experimental and computational is observed at a heat flux of 100.41 W/m^2, the deviation after that from a heat flux of 172.87 to 376.14 W/m^2 is only 1.4 %. Therefore, excluding the lowest heat flux of 100.41 W/m^2, the computational results obtained are extremely close to the experimental values for temperature between evaporator and condenser.

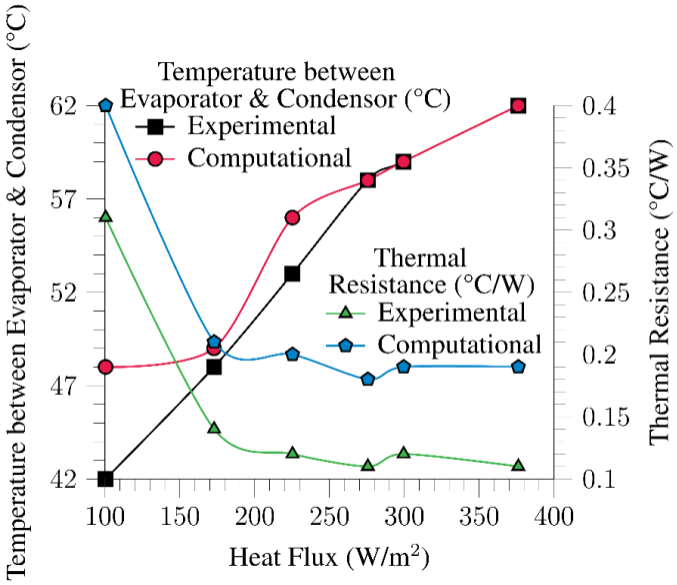

Figure 5 Validation of computational results with experimental results of Fadhl *et al*. [37].

Results and discussion

Effect of heat flux and concentrations of nanoparticles on thermal efficiency

The highest thermal efficiency in **Figure 6** is 50 % at 500 W/m^2 heat flux for 0.1 % Ag. The thermal efficiency of 0.1 % Ag is lower at lower heat flux and it becomes the highest at high heat flux. The thermal efficiency of the nanofluids observed increases with a rise in heat flux from 100 to 500 W/m^2. The highest average thermal efficiency is observed for 3 % CuO is 40.3 % and the least average thermal efficiency is observed for 0.1 % Ag is 30.8 %. Except for 0.1 % Ag, the thermal efficiency of the nanofluids observed in **Figure 6** are crowded together and deviate very little from each other.

Dispersing nanoparticles increase both the thermal conductivity and viscosity of the PCM. Thermal conductivity increase improves the heat conduction to PCM and viscosity enhancement reduces the flow intensity, consequent to natural convection. The addition of nanoparticles, in general, did not have a major impact on system heat transfer as the increase in the melted PCM inside the U tube was found to be 5 % after 180 min using 0.2 % Ag nanoparticles. Increasing working media temperature by 5 °C from 70 to 75 °C increased the melted PCM inside the U tube by 17 % after 180 min.

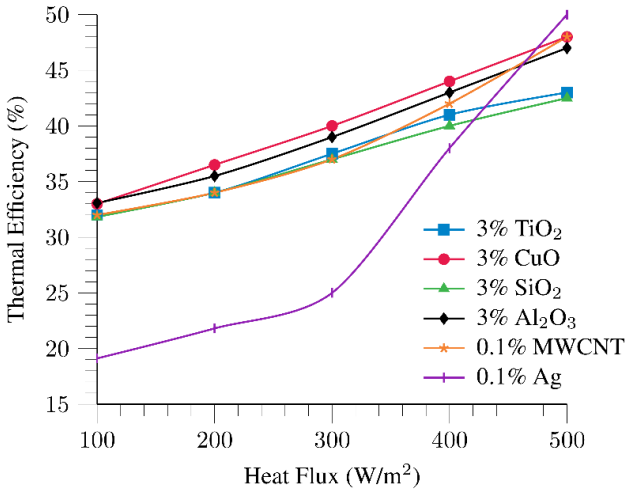

Figure 6 Thermal efficiency for different heat flux and concentrations of nanoparticles.

Effect of tilt angle and fill ratio on heat transfer coefficient

A fill ratio of 60 % has the highest heat transfer coefficient at 7,800 W/m^2.K and a tilt angle of 65° and 70° results in the highest heat transfer rate at 7,800 W/m^2.K (**Figure 7**). Even though the heat transfer coefficient at 65° and 70° are the same, a lower tilt angle is preferred.

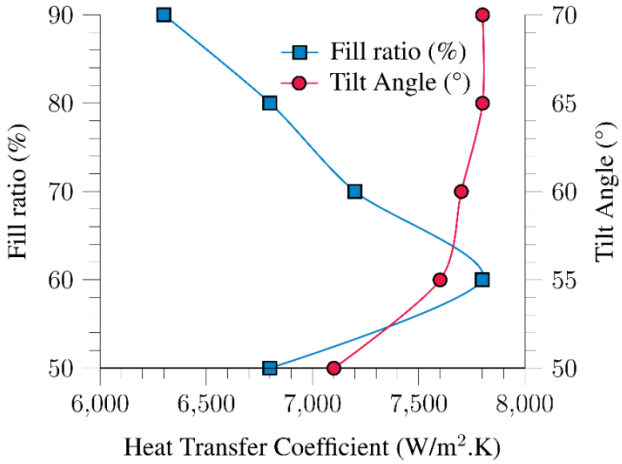

Figure 7 Effect of tilt angle and fill ratio on heat transfer coefficient.

Thermal resistance lowered with nanofluids at FR of 50 % and 100 W when the TPCT was operating with MWCNT nanofluid at 0.1 %. This reduction might be due to the nanoparticles floating on the vapour bubbles upon their formation and later breaking them. Similar values of thermal resistance at FR 60 % when using nanofluid might be due to the nucleate pool boiling by the expansion of nanofluid. Bubble departure frequency enhancement and reduction in bubble departure diameter resulted in fluid expansion due to the increase in the number of smaller bubbles and creates flow resistance. Further, nanoparticle collision enhances surface, roughness, and turbulence. The heat transfer performance of closed thermosyphon assuming a 2-phase system, working at various heat input, inclination angles, and filling ratios show that an increase in the heating power input decreased the efficiency. Similar results are published by Solomon *et al*. [38] and Karthikeyan *et al*. [39].

The optimum tilt angle of heat pipe is the one having maximum impact of gravity on the working media flow between the condenser and the evaporator. The condenser receives additional condensation at 50 % fill ratio and the temperature gets reduced [40]. The thermosyphon signifies a lower system thermal resistance and hence operates as the best at 50 % fill ratio [37]. As the cooling water flow rate enhances, gain in heat energy from the condenser also enhances leading to a lowering of the condenser surface area.

Effect of different nanoparticles and heat flux on heat transfer coefficient

Figure 8 shows that the heat transfer coefficient increases with an increase with heat flux for 0.2 % Ag and 0.2 % MWCNT. 0.2 % Ag has a 1.95 % higher average heat transfer coefficient than 0.2 % MWCNT. The highest heat transfer coefficient reported for 0.2 % Ag is 7745 W/m^2.K.

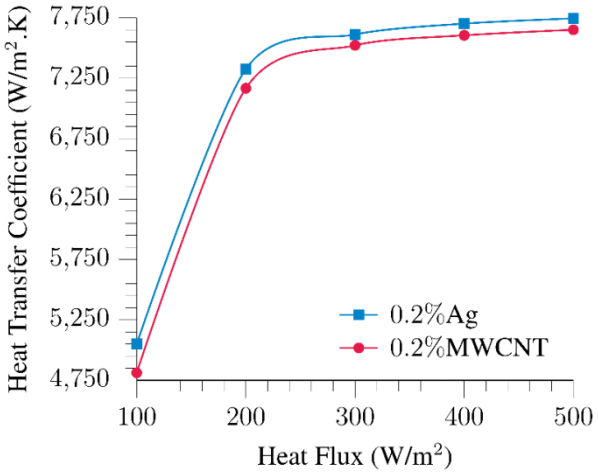

Figure 8 Comparison of heat transfer coefficient for 0.2 % Ag and MWCNT for different heat flux.

The heat transfer coefficient increases at a higher rate from 100 to 200 W since the nucleate boiling is initiated and augmented by the Brownian motion and micro-cavity filling by the nanoparticles, in place of vapour. Dispersing nanoparticles enhanced PCM's thermal conductivity and viscosity. The former enhanced the PCM heat conduction, whereas the latter decreased the flow intensity consequent to natural convection.

Effect of different nanoparticles and heat flux on temperature between condenser and evaporator and difference in temperature

As the heat flux rises from 100 to 500 W/m^2 (**Figure 9**), the difference in temperature and the temperature between condenser and evaporator increases. Average temperature difference is higher for 0.2 % Ag at 76.8 °C and is at 69.2 °C for 0.2 % MWCNT. The average temperature between evaporator and condenser is 130.2 °C for 0.2 % Ag and 113.6 °C for 0.2 % MWCNT.

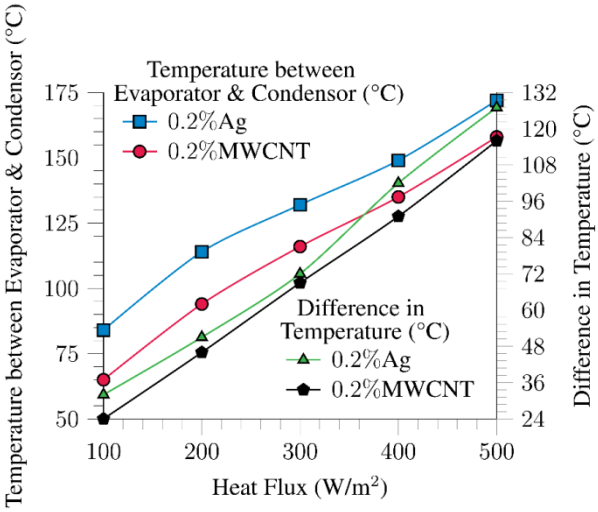

Figure 9 Temperature between evaporator and condenser and the difference in temperature for different heat flux using 0.2 % Ag and MWCNT nanoparticles.

The addition of nanoparticles results in its aggregation as a barrier in the adiabatic section at low heat input, and constant geyser boiling. The expansion of the working media in this study might be the result of increased departure of bubbles and lower bubble growth as reported earlier [41]. This results in a similar profile of temperature in the adiabatic section and evaporator as the nanofluid fills in these 2 sections and hence prevents the condensate flow to evaporator by creating a thermal resistance.

Effect of different nanoparticles and heat flux on thermal resistance and thermal efficiency

In **Figure 10**, it is observed that the thermal efficiency increases as heat flux increases from 100 to 500 W/m^2 and the thermal resistance decreases. Average thermal efficiency is 38.9 % for 0.2 % Ag and 43 % for 0.2 % MWCNT. Average thermal resistance is 0.188 for 0.2 % Ag and 0.178 for 0.2 % MWCNT. Thermal resistance decreases with heat flux non-linearly as the heat transfer mechanism changes to nucleate boiling from convection.

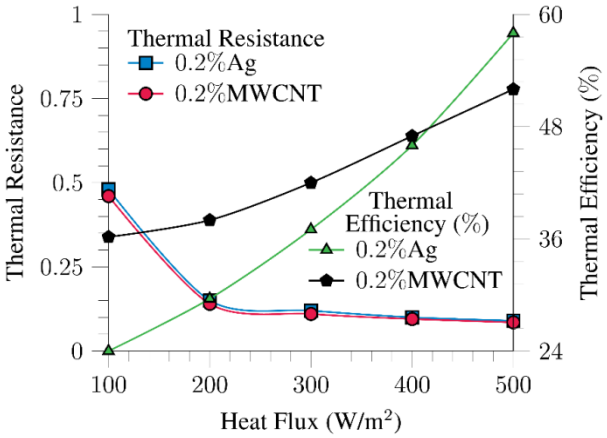

Figure 10 Thermal resistance and efficiency for different heat flux, using 0.2 % Ag and MWCNT nanoparticles.

Effect of nanoparticles on thermal efficiency at different Re

Thermal efficiency increases till Reynolds number 10,000 and decreases after it. Average thermal efficiency of 0.2 % Ag is 89.6 % and 73.3 % for 0.2 % MWCNT. The highest thermal efficiency is 92 % for 0.2 % Ag at Re 10,000. The thermal efficiency of 0.2% Ag is much higher than that of 0.2 % MWCNT at all Reynolds numbers as shown in **Figure 11**.

The thermal efficiency is not influenced by the change in Re from 500 to 1,000 as well as from Re 2,500 to 30,000 as the enhancement in thermal efficiency is only 4 %. The same is the case with the use of different collector materials such as steel, Aluminium, and Copper. With respect to the change in the ratio of tube width to spacing, when the hydraulic diameter is kept constant, the tube width should be ideally kept equal to spacing or higher, as the change in thermal efficiency is only 1.2 %.

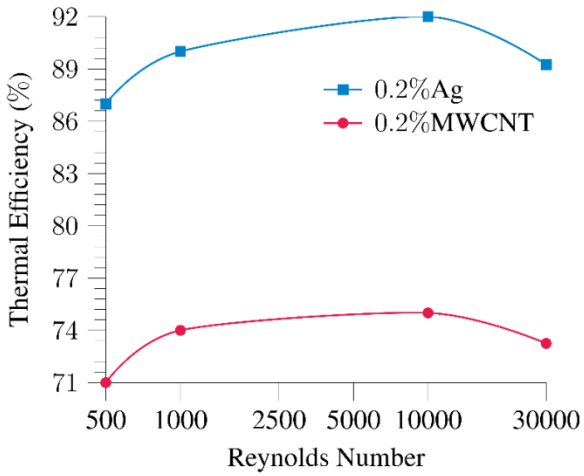

Figure 11 Thermal efficiency at different Re, using 0.2 % Ag and MWCNT nanoparticles.

The U heat pipe transfers the heat collected from the sun up to the manifold, where cold water passes through. The working of a heat pipe of a reverse thermosyphon is underlined on the evaporation/ condensation phenomena of a small droplet of working media inside, where when heated the working media evaporates to the top of the heat pipe and as it condenses gravity pulls it back to the bottom.

The CFD modeling of the solar thermal collector was initialized with the flat-lining of fin temperature begins at 25 min of data collection. This is due to the latent heat release from PCM Erythritol once the temperature in the tube is below the solidus temperature, as reported by Shen *et al*. [42], Coccia *et al*. [18] and Anish *et al*. [17]. As PCM Erythritol solidifies, latent heat is being released into the tube collectors, hence keeping the fin at a constant temperature. After 120 min, PCM Erythritol is solidified completely, hence the fin temperature once again experiences a steeper drop as there is no more latent heat being released into the system. The solar thermal collector exhibits enhanced performance as it maintains a higher fin temperature due to the U-tube characterization. The solar thermal collector demonstrates a higher amount of sensible heat inside the tube due to the high specific heat capacity as well as a large amount of the selected working media. This results in larger heat extraction from the tube, therefore, faster initiation of the solidification process of PCM Erythritol. Consequently, the large amount of stored heat will be released back to the tube, keeping the fin temperature at a higher value. In addition to latent heat energy from the PCM Erythritol which acts as a backup heat, the solar thermal collector system has a significant amount of sensible heat energy from the erythritol flowing through the U-tube inside the tube collectors. Different compositions of erythritol, Ag, and MWCNT nanoparticles were employed as nano-encapsulated PCMs.

Temperature and pressure variations using heat flux 500 W and 0.2 % MWCNT

For 0.2 % MWCNT at 10 m for a flow rate of 20 L/s at a heat flux of 500 W the vapour, liquid, and storage tank temperature is 29, 48 and 19 °C, respectively (**Table 2**). The vapour pressure is observed to be 0.8 bar.

Hoseinzadeh *et al*. [43] reported that a linear direct relation is observed experimentally with the use of water for difference in temperature of the thermosyphon and heat flux whereas with the use of nanofluid, the difference in temperature fluctuates with the heat flux. Further, with the same heat flux, temperature difference of the thermosyphon by using nanofluid was lower than that of using water. The inference was at a fixed difference in temperature of the thermosyphon, nanofluid employs higher heat flux than that for water. Same curve characteristics have been observed for temperature difference of the thermosyphon on using nanofluid and after reaching a maximum value, stable values are observed over time.

The period of a cycle of work is decided by the variation in temperature and pressure. During the time of heat transfer from the hot to the cold section, the pressure and temperature is increased and this corresponds to the pumping cycle. The liquid return corresponds to the lowering of pressure and temperature. Soon after the reverse thermosyphon starts operation, the water temperature of the condenser and liquid temperature lowers. The level difference of liquid is lowest at the beginning and highest at the end of pumping cycle, followed by the return of liquid. The vapour pressure difference at the end of the pumping cycle equals liquid lifting pressure and is not influenced by the heat flux and height of heat transport. Eventually, the vapour pressure difference is decided by the height of the liquid lift.

Table 2 At 10 m after operation, at heat flux 500 W and liquid flow rate 20 L/s using 0.2 % MWCNT.

Parameters	Temperature /Pressure
Vapour temperature	29 °C
Liquid temperature	48 °C
Storage tank temperature	19 °C
Vapour pressure	0.8 bar

The lowest heat flux registered the lowest pressure difference and the highest heat flux recorded the highest-pressure difference. As the heat flux increases, the intensity of evaporation increases, and the flow rate of the medium in the condenser that carries the heat also increases. Higher heat flux results in a lower loss of heat and there observed no relation between the heat loss and the heat flux.

Effect of storage tank and ambient temperature difference on heat losses in the system

For 0.2 % MWCNT, the heat loss increases with the difference in temperature between storage tank and ambient (**Table 3**).

Table 3 Heat Loss (kJ) in the system using 0.2 % MWCNT.

Difference in temperature between storage tank and ambient (°C)	Heat Loss (KJ)
5	1,250
15	1,750
25	2,750
35	4,500

In the U-tube solar thermal collector system, the higher the heat transfer rate, the more heat is being extracted to the liquid medium on the condenser section. It can be predicted that using working media with enhanced thermophysical properties in this system configuration will release more heat at the condenser to provide more heat to the demand side. This consequently lowers the fin temperature in the tube collector. By using materials with higher specific heat capacity and thermal conductivity as in working media, the lower the overall fin temperature of the system is obtained. As higher fin temperature in the solar thermal collector configuration shows that their latent heat storage is being released from the PCM into the U pipe, providing heat for an extended period of time when there is no sun available in a stagnation operation, and improve the functionality of the system. The lower fin temperature is because the amount of heat transferred to the liquid medium cannot be balanced by the amount of heat provided by the PCM inside the tube collector - there is more heat being transferred to the demand side than there is the amount of heat being released to the U-tube inside the solar thermal collector from the PCM in each loop, therefore resulting in lower fin temperature for working media that has higher thermal conductivity and specific heat capacity.

Phase change phenomena during evaporation in the heat pipe

Experimental work is conducted using a simple heat pipe of similar geometry as that of the reverse thermosyphon with a heat flux of 100 - 500 W at fill ratio 60 %, Tilt angle 65° using water, and 0.2 % Ag and MWCNT with erythritol. The heat flux was provided with a manually changing resistance fitted heater. An equilibrium condition could be noticed soon after an elapse of 40 min. The elevated condenser temperature and reverse thermosyphon boiling limit of dry-out using water (**Figure 12(a)**) were eliminated

by using 0.2 % Ag and MWCNT nanoparticles. A substantial working media expansion, consequent to the nucleate pool boiling, could be noticed, using 0.2 % Ag and MWCNT nanoparticles 100 - 500 W heat flux and fill ratios above 60 % (**Figure 12(b)**).

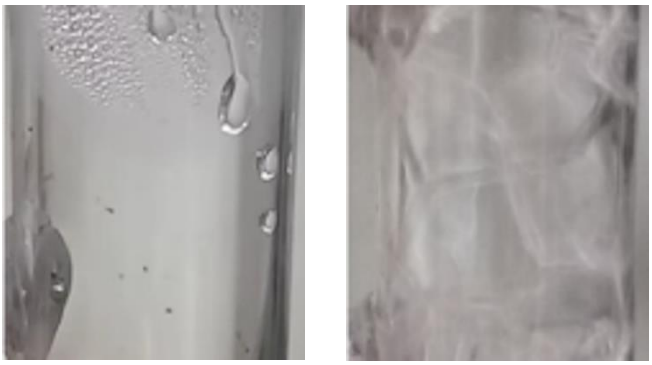

(a) **(b)**

Figure 12 Phase change phenomena during evaporation in heat pipe; a) Dry-out limit b) Expansion of working media.

Water is observed to reach the dry out limit in the parametric operation limits of 100 - 500 W heat flux, fill ratio 60 % and tilt angle 65°. For 0.2 % MWCNT and 0.2 % Ag in the same parametric operation limits the working media expands and no nanoparticle barrier and geyser boiling is observed (**Table 4**). Hence, no additional thermal resistance is characterized with the use of nanofluid. Nanoparticle barrier prevents movement of vapour to condenser and that of condensate from the condenser to evaporator that causes additional thermal resistance. Geyser boiling could not be observed using nanofluid/water with all the input powers (100 **-** 500 W**)** and no large bubble collapses there. Hence no change in the thermosyphon wall temperature and resistance to heat transfer is noticed. The thermal efficiency is thus enhanced to approximately 10 - 15 % higher for nanofluids than when water was employed.

Table 4 Experimental parametric operation limits at 100 - 500 W heat flux, fill ratio 60 %, tilt angle 65° in the heat pipe.

Heat transfer fluid	**Observed phenomenon**
Water	Dry-out limit
0.2 % MWCNT	Expansion of working media, No nanoparticle barrier, and geyser boiling observed
0.2 % Ag	Expansion of working media, No nanoparticle barrier, and geyser boiling observed

The evaporator temperature was enhanced by using nanofluid at fill ratios of 30 and 45 %. The reason for this behaviour is limiting the maximum amount of evaporator heat leading to a boiling limit of dry-out. The adiabatic section shows a characteristic drying area. With fill ratios of 45 % and using 0.2 % of Ag/MWCNT, the evaporator temperature was lowered at low input powers and the expansion of the working media occurs to the entire evaporator, which improved the operation. Khazaee *et al*. [44] reported the reason for the fluctuations in temperature is due to the geyser boiling. Rise in thermal resistance due to the combined effect of the sensible as well as latent heat, and the performance in heat transfer is found to be lower in comparison to the nucleate pool boiling phenomenon [45,46]. Tecchio *et al*. [46] reported a reduction in the thermal performance since large bubbles collapse. Jafari *et al*. [47] reported the omission of dry-out limit and geyser boiling at FRs under 35 %.

A similar result at a 60 % FR is contradictory to Hoseinzadeh *et al*. [43] who found a negligible reduction in evaporator temperature as nanoparticle concentration increased. The nanoparticle barrier covering the adiabatic section is consequent to the addition of Al_2O_3 nanoparticles at 0.5 wt.%, at a heat

flux of 40 W, and continued geyser boiling. Water requires an amount of heat for evaporation equal to about 2.4 MJ/kg, which is a high amount of energy required to evaporate 1 kg of water comparing to nanofluids (about 0.2 MJ/kg). The CFD model exhibited the difference in pool boiling behaviour between nanofluid and water.

The effective thermal conductivity gets lowered by 10 % for 1 % Ag-H_2O nanofluid compared to water. Thermal conductivity of Ag nanofluids was found to be temperature dependent, owing to the suppression of molecular H bonding between the molecules of water above a threshold concentration [48]. Layering at the liquid-solid interface, agglomeration of nanoparticles leading to the formation of linear chain-like structure, and the high surface thermal conductance of silver-water interfaces (low interfacial or Kapitza resistance) might influence thermal conductivity enhancement of Ag nanofluids at reported low concentrations [49]. Within the reported specific low concentration range of the Ag nanoparticles, the absorbance/catalytic activity of horseradish peroxidase (HRP) enzyme activity not only gets enhanced, but also alter the structure favourably. There was a maximum increase in ellipticity and a-helix contents (demonstrated by circular dichroism fluorescence spectra) as well at this concentration. Above and below this concentration range, there was a decrease in the activity of HRP [50].

The saturated vapour moves into the condenser through the adiabatic section. As the saturated vapour contacts the condenser's surface, where the temperature is below the saturation temperature of the vapour, the cold walls of the condenser show liquid film, as vapour condenses. The film of liquid fall through the condenser to the evaporator. During the above cycle, latent heat absorbed in the evaporator is released by the vapour and transferred through the liquid film to the wall of the condenser, where a boundary condition of convection heat transfer is imposed. working media requires very low latent heat of vaporization (up to the order of one-tenth that of water) in order to evaporate an equal quantity of working media compared to water, which requires much higher latent heat of vaporization.

Conclusions

The low-boiling medium in liquid form returns gravitationally along with the condensate line to the evaporator. Reverse thermosyphons with 2 working media and a bubble pump were successfully carried out with numerical studies using solar thermal collector as the heat source with finned U-tube for heat transfer. The tests proved that a continuous operation of thermosyphons with heat input from 100 to 500 W is feasible.

Thermal resistance and thermal efficiency using 6 different nanofluids at 0.1 - 3 % concentrations with erythritol as PCM and tri ethanol amine as dispersant at Re 500 - 30,000 and heat flux 100 - 500 W. MWCNT at 0.2 % concentration was adjudged the best from heat flux 100 - 400 W and thereafter, 0.2 % Ag was found the best. The tilt angle and fill ratio effects on heat transfer coefficient at different heat flux concluded with a better performance at 65° and 60 % fill ratio. The temperature between evaporator and condenser and the difference in temperature at different heat flux and its reflection on the thermal performance of the system is evaluated. Repeated pressure and temperature variation expressing the work periods are presented. Heat losses in the system, using MWCNT at 0.2 % concentration was found. Phase change phenomena during the evaporation in heat pipe experimentally with similar geometry and boundary conditions to that of numerical studies could highlight the differences in the boiling limit of dry-out and the working media expansion while using water and nanofluid respectively. The results are pictorially represented and scientifically discussed in the manuscript.

This study provides evidence that the proposed CFD model of a bubble pump enabled reverse thermosyphon with a 2-dimensional geometry has successfully reproduced both the characteristics of fluid flow as well as thermodynamics. The model depicts compounded phenomena of physical nature such as heat and mass transfer. The heat transfer involves both the evaporation and condensation processes. The mass transfer involves a phase change both from the liquid to vapour and from vapour to liquid in the course of the pool boiling and film condensation, respectively. The results demonstrate the abilities of the CFD model to simulate the characteristics of multiphase flow for different working media. A good agreement has been observed at similar conditions between the predicted CFD and experimental temperature profiles along the reverse thermosyphon. CFD thermal performance of the reverse thermosyphon has also successfully emphasized the variation trends of the experimental measurements for different power throughputs.

The results demonstrated that the effect of Ag/MWCNT nanoparticle's impact on natural convection in flows lowers due to the enhanced viscosity. The effect of Ag/MWCNT nanoparticles in PCM thermal conductivity increase was lower in the liquid phase than in the solid phase. The novelty of this study is the reduced rate of heat loss, increased rate of energy storage by integrating PCM directly inside the tube, and

finally enhanced rate of heat transfer by incorporating a working media with high heat capacity. The selection of a suitable working media is vital as it contributes to improving system efficiency and consequently reduces the cost of operation.

References

[1] JA Alfaro-Ayala, G Martinez-Rodriguez, M Picon-Nunez, AR Uribe-Ramirez and A Gallegos-Munoz. Numerical study of a low temperature water-in-glass evacuated tube solar collector. *Energy Convers. Manag.* 2015; **94**, 472-81.

[2] T Bouhal, Y Agrouaz, T El Rhafiki, Y Zeraouli and A Jamil. Towards an energy efficiency optimization of solar horizontal storage tanks and circulation pipes integrating evacuated tube collectors through CFD parametric studies. *Sustain. Energy Technol. Assess.* 2018; **26**, 93-104.

[3] MA Essa and NH Mostafa. Theoretical and experimental study for temperature distribution and flow profile in all water evacuated tube solar collector considering solar radiation boundary condition. *Sol. Energy* 2017; **142**, 267-77.

[4] S Fertahi, T Bouhal, T Kousksou, A Jamil and A Benbassou. Experimental study and CFD thermal assessment of horizontal hot water storage tank integrating evacuated tube collectors with heat pipes. *Sol. Energy* 2018; **170**, 234-51.

[5] M Iranmanesh, HS Akhijahani and MSB Jahromi. CFD modeling and evaluation the performance of a solar cabinet dryer equipped with evacuated tube solar collector and thermal storage system. *Renew. Energy* 2020; **145**, 1192-213.

[6] A Ozsoy and V Corumlu. Thermal performance of a thermosyphon heat pipe evacuated tube solar collector using silver-water nanofluid for commercial applications. *Renew. Energy* 2018; **122**, 26-34.

[7] S Qiu, M Ruth and S Ghosh. Evacuated tube collectors: A notable driver behind the solar water heater industry in China. *Renew. Sust. Energ. Rev.* 2015; **47**, 580-8.

[8] M Sabiha, R Saidur, S Mekhilef and O Mahian. Progress and latest developments of evacuated tube solar collectors. *Renew. Sust. Energy Rev.* 2015; **51**, 1038-54.

[9] J Zeng and Y Xuan. Enhanced solar thermal conversion and thermal conduction of MWCNT-SiO_2/Ag binary nanofluids. *Appl. Energy*. 2018; **212**, 809-19.

[10] GR Challa, M Natarajan and A Palayakkodan. Experimental study on performance enhancement of evacuated tube by constant heat flux mode. *Appl. Solar Energy* 2018; **54**, 40-9.

[11] Y Wu, J Li, M Wang, H Wang, Y Zhong, Y Zhao, M Wei and Y Li. Solar salt doped by MWCNTs as a promising high thermal conductivity material for CSP. *R. Soc. Chem. Adv*. 2018; **8**, 51-19260.

[12] A Fernandez, H Galleguillos, E Fuentealba and F Perez. Thermal characterization of HITEC molten salt for energy storage in solar linear concentrated technology. *J. Therm. Anal. Calorim.* 2015; **122**, 3-9.

[13] MMA Khan, NI Ibrahim, I Mahbubul, HM Ali, R Saidur and FA Alsulaiman. Evaluation of solar collector designs with integrated latent heat thermal energy storage: A review. *Sol. Energy* 2018; **166**, 334-50.

[14] N Kumar, J Hirschey, TJ Laclair, KR Gluesenkamp and S Graham. Review of stability and thermal conductivity enhancements for salt hydrates. *J. Energy Storage* 2019; **24**, 1-15.

[15] X Peng, M Yao, TW Root and CT Maravelias. Design and analysis of concentrating solar power plants with fixed-bed reactors for thermochemical energy storage. *Appl. Energy* 2020; **262**, 114543.

[16] FL Rashid and A Hashim. Development of phase change materials/ nanoparticles for thermal energy storage: Review. *Int. J. Sci. Res*. 2020; **3**, 790-9.

[17] R Anish, V Mariappan, MM Joybari and AM Abdulateef. Performance comparison of the thermal behavior of xylitol and erythritol in a double spiral coil latent heat storage system. *Therm. Sci. Eng. Prog.* 2020; **15**, 100441.

[18] G Coccia, A Aquilanti, S Tomassetti, G Comodi and GD Nicola. Design, realization, and tests of a portable solar box cooker coupled with an erythritol-based PCM thermal energy storage. *Sol. Energy* 2020; **201**, 530-40.

[19] S Guo, Q Liu, J Zhao, G Jin, X Wang, Z Lang, W He and Z Gong. Evaluation and comparison of erythritol-based composites with addition of expanded graphite and carbon nanotubes. *Appl. Energy* 2017; **205**, 703-9.

[20] R Farjallah, M Chaabane, H Mhiri, P Bournot and H Dhaouadi. Thermal performance of the U-tube solar collector using computational fluid dynamics simulation. *J. Sol. Energy Eng.* 2016; **138**, 061008.

[21] H Kaya and K Arslan. Numerical investigation of efficiency and economic analysis of an evacuated U-tube solar collector with different nanofluids. *Heat Mass Transf.* 2019; **55**, 581-93.

[22] K Vignarooban, X Xu, A Arvay, K Hsu and A Kannan. Heat transfer fluids for concentrating solar power systems – A review. *Appl*. *Energy* 2015; **146**, 383-96.
[23] Y Wang, L Wang, N Xie, X Lin and H Chen. Experimental study on the melting and solidification behavior of erythritol in a vertical shell-and-tube latent heat thermal storage unit. *Int*. *J. Heat Mass Transf*. 2016; **99**, 770-81.
[24] Y Wang, S Li, T Zhang, D Zhang and H Ji. Supercooling suppression and thermal behavior improvement of erythritol as phase change material for thermal energy storage. *Sol. Energy Mater. Sol. Cells* 2017; **171**, 60-71.
[25] MH Zahir, SA Mohamed, R Saidur and FA Al-Sulaiman. Supercooling of phase-change materials and the techniques used to mitigate the phenomenon. *Appl*. *Energy* 2019; **240**, 793-817.
[26] A Fluent. *Ansys Fluent 2020 R1-Theory Guide; User's Guide*. Canonsburg, PA, USA, 2020.
[27] VR Pawar and S Sobhansarbandi. CFD modeling of a thermal energy storage-based heat pipe evacuated tube solar collector. *J*. *Energy Storage*. 2020; **30**, 101528.
[28] HC Hottel and A Whillier. Evaluation of fat plate collector performance. *In:* Proceedings of the Conference on the Use of Solar Energy, University of Arizona Press, 1958, p. 74.
[29] RW Bliss. The derivation of several plate efficiency factors useful in the design of flat plate solar heat collectors. *Sol. Energy* 1959; **3**, 55-64.
[30] A Whillier. *Design factors influencing collector performance, low temperature engineering*. *In:* RC Jordan (Ed.). Application of solar energy. ASHRAE, New York, 1967.
[31] JAD William and A Beckman. Solar engineering of thermal processes. 4th eds. John Wiley & Sons, Inc., Hoboken, New Jersey, 1980, p. 928.
[32] JA Duffie and WA Beckman. *Solar engineering of thermal processes*. 4th eds. Hoboken, New Jersey: John Wiley & Sons, Inc., Hoboken, New Jersey, 2013.
[33] MG Mousa. Effect of nanofluid concentration on the performance of circular heat pipe. *Ain Shams Eng. J*. 2011; **2**, 63-9.
[34] P Hanafizadeh, A Karimi and MH Saidi. Effect of step geometry on the performance of the airlift pump. *Int. J. Fluid Mech. Res.* 2011; **38**, 387-408.
[35] A Papadimitratos, S Sobhansarbandi, V Pozdin, A Zakhidov and F Hassanipour. Evacuated tube solar collectors integrated with phase change materials. *Sol Energy* 2016; **129**, 10-19.
[36] V Hernandez-Perez, M Abdulkadir and B Azzopardi. Grid generation issues in the CFD modelling of two-phase flow in a pipe. *J. Comput. Multiph. Flows.* 2011; **3**, 13-26.
[37] B Fadhl, LC Wrobel and H Jouhara. Numerical modelling of the temperature distribution in a two-phase closed thermosyphon. *Appl. Therm. Eng.* 2013; **60**, 122-31.
[38] AB Solomon, R Roshan, W Vincent, VK Karthikeyan and LG Asirvatham. Heat transfer performance of an anodized two-phase closed thermosyphon with refrigerant as working fluid. *Int. J. Heat Mass Transfer*. 2015; **82**, 521-9.
[39] M Karthikeyan, S Vaidyanathan and B Sivaraman. Thermal performance of a two phase closed thermosyphon using aqueous solution. *Int. J. Eng. Sci. Technol.* 2010; **2**, 913-8.
[40] RS Nair and C Balaji. Synergistic analysis of heat transfer characteristics of an internally finned two phase closed thermosyphon. *Appl. Therm. Eng.* 2016; **101**, 720-9.
[41] G Hetsroni, JL Zakin, Z Lin, A Mosyak, EA Pancallo and R Rozenblit. The effect of surfactants on bubble growth, wall thermal patterns and heat transfer in pool boiling. *Int. J. Heat Mass Transf*. 2001; **44**, 485-97.
[42] S Shen, S Tan, S Wu, C Guo, J Liang, Q Yang, G Xu and J Deng. The effects of modified carbon nanotubes on the thermal properties of erythritol as phase change materials. *Energy Convers. Manag*. 2018; **157**, 41-8.
[43] S Hoseinzadeh, SAR Sahebi, R Ghasemiasl and AR Majidian. Experimental analysis to improving thermosyphon (TPCT) thermal efficiency using nanoparticles/based fluids (water). *Eur. Phys. J. Plus*. 2017; **132**, 197.
[44] I Khazaee, R Hosseini and SH Noie. Experimental investigation of effective parameters and correlation of geyser boiling in a two-phase closed thermosyphon. *Appl. Therm. Eng.* 2010; **30**, 406-12.
[45] K Smith, S Siedel, AJ Robinson and R Kempers. The effects of bend angle and fill ratio on the performance of a naturally aspirated thermosyphon. *Appl. Therm. Eng.* 2016; **101**, 455-67.
[46] C Tecchio, JLG Oliveira, KV Paiva, MBH Mantelli, R Galdolfi and LGS Ribeiro. Geyser boiling phenomenon in two-phase closed loop-thermosyphons. *Int. J. Heat Mass Tran.* 2017; **111**, 29-40.
[47] D Jafari, S Filippeschi, A Franco and PD Marco. Unsteady experimental and numerical analysis of a two-phase closed thermosyphon at different filling ratios. *Exp. Therm. Fluid Sci.* 2017; **81**, 164-74.

[48] M Seyhan, CL Altan, B Gurten and S Bucak. The effect of functionalized silver nanoparticles over the thermal conductivity of base fluids. *AIP Adv.* 2017; **7**, 045101.
[49] G Paul, S Sarkar, T Pal, PK Das and I Manna. Concentration and size dependence of nano-silver dispersed water based nanofluids. *J. Colloid Interface Sci.* 2012; **371**, 20-7.
[50] Z Karim, R Adnan and MS Ansari. Low concentration of silver nanoparticles not only enhances the activity of horseradish peroxidase but alter the structure also. *PLoS One* 2012; **7**, e41422-1-8.